PHYSICAL REVIEW E **103**, 012603 (2021)

Relation between dilation and stress fluctuations in discontinuous shear thickening suspensions

Rijan Maharjan, Ethan O'Reilly, Thomas Postiglione, Nikita Klimenko, and Eric Brown[*]
Department of Mechanical Engineering and Materials Science, Yale University, New Haven, Connecticut 06520, USA

(Received 29 April 2020; revised 26 November 2020; accepted 17 December 2020; published 7 January 2021)

We investigate dilation-induced surface deformations in a discontinuous shear thickening (DST) suspension to determine the relationship between dilation and stresses in DST. Video is taken at two observation points on the surface of the suspension in a rheometer while shear and normal stresses are measured. A roughened surface of the suspension is observed as particles poke through the liquid-air interface, an indication of dilation in a suspension. These surface roughening events are found to be intermittent and localized spatially. Shear and normal stresses also fluctuate between high- and low-stress states, and surface roughening is observed frequently in the high-stress state. On the other hand, a complete lack of surface roughening is observed when the stresses remain at low values for several seconds. Surface roughening is most prominent while the stresses grow from the low-stress state to the high-stress state, and the roughened surface tends to span the entire surface by the end of the stress growth period. Surface roughening is found only at stresses and shear rates in and above the shear thickening range. These observed relations between surface roughening and stresses confirm that dilation and stresses are coupled in the high-stress state of DST.

DOI: 10.1103/PhysRevE.103.012603

I. INTRODUCTION

Discontinuous shear thickening (DST) is a macroscopic behavior of a fluid in which the apparent viscosity increases sharply as a function of shear rate in steady-state flows. DST is generally found in suspensions of hard particles without strong interparticle forces, and at packing fractions just below the liquid-solid transition (for a review, see Ref. [1]). DST is often described as a transition from a low-stress state to a high-stress state, which occurs when shear forces overcome interparticle forces to cause contact and friction to form system-spanning contact networks [2–4]. The stress in the low-stress state can be dominated by hydrodynamic forces [4,5], weak repulsive forces [6,7], attractive forces [8], or other interparticle forces such as the weight of settled particles [2]. The high-stress state is usually described as frictional. The most popular model proposes that the high-stress state is a hybrid viscous-frictional internal bulk state where shear stresses are proportional to both normal stresses and shear rate [4]. In contrast with this model, we argue that shear stress in the high-stress state is only proportional to the normal stress, and the macroscopic behavior in the high-stress state is determined by this constitutive relation in combination with the stiffness of the boundary (e.g., from surface tension), as it provides a restoring force in response to dilation [2]. To demonstrate the connection between stress and surface deformations due to dilation, we report rheological measurements along with video of the surface of a DST suspension.

It has long been claimed that DST in suspensions occurs along with Reynolds dilatancy, so much so that they are sometimes used as synonyms for each other [9,10]. Reynolds dilatancy is an expansion in the volume of a dense particle packing in response to shear. As particles try to move past each other in a dense packing, they push against each other and the volume taken up by the particle packing tends to expand, so that once a steady flow is reached, it is at a lower packing fraction than it was initially prepared. In a suspension, the liquid migrates from the surface to fill the larger volume in the interstices between particles that also expand along with the particle packing during dilation. This is visible on the surface of the suspension as particles poke through the liquid-air interface to make the surface rough. This roughened surface reflects light diffusively and appears matte when the particles are too small to see by the naked eye but larger than around the wavelength of light. As a shorthand, we refer to this phenomenon of the visibly roughened surface as "surface roughening," as it is a convenient visual indicator of overall dilation.

Dilatancy has been proposed to play an important role in DST [2]. When material dilates, it pushes against the boundary. The boundary then responds with a restoring force. Assuming the particles are harder than the least stiff boundary, the least stiff boundary is expected to determine the scale of the normal stress. Typically the least stiff boundary in a dense suspension flow is the liquid-air interface, in which case dilation causes particles to poke through the liquid-air interface [2,11]. This deforms the liquid-air interface, ultimately resulting in a minimum radius of curvature on the order of the particle size, which visually appears as surface roughening. Surface tension provides a normal stress pushing back on the particles with a maximum on the order of surface tension divided by particle size [2,11–13]. The maximum stress supported in the shear thickening range has been shown to agree with this order-of-magnitude scaling for dozens of suspensions [1,2]. This normal stress is transmitted from particle to

---

[*] ericmichealbrown@gmail.com

particle along frictional contacts to provide resistance to shear, in system-spanning networks that repeatedly form and break up while the system is sheared.

Since dilation represents an expansion, dilation is often associated with normal stresses pushing against rheometer plates. Normal stresses pushing against rheometer plates are reported in numerous experiments (for a summary, see Ref. [1]). A few measurements of dilation based on volumetric change in DST suspensions exist as well. Volumetric expansion at the liquid-air interface has been measured with a camera to be up to about one particle diameter, and was found to follow a predicted function of shear stress due to surface tension in response to dilation [2]. In a variation on the typical fixed-gap rheometer experiment, controlled normal stress experiments which allowed the rheometer gap to vary measured a volumetric expansion with shear [14]. While positive normal stress and corresponding dilation have been observed in DST suspensions, these observations do not distinguish whether stresses are determined by bulk flow or the boundary condition.

Published images of surface roughening in DST suspensions are rare. Some of the early work discussing the relation between dilatancy and shear thickening is summarized by claims (but no images) that visible dilatancy at the surface of suspensions was observed starting at the same shear rate that shear thickening starts [9]. Some published images of DST suspensions show protuberances on the surface indicative of normal stress pushing outward [15,16], but these appear to be a different surface instability than the poking of particles through the liquid-air interface that is predicted to be relevant to the measured stress [2]. A closeup view of a suspension surface with a microscope showed particles poking through the liquid-air interface under shear in the high-stress state [2,17], but this has only been shown at one applied stress. Thus, while there are many claims, no evidence has been published which shows that the parameter range of DST coincides with the parameter range of visible surface roughening.

Perhaps the best images of what a dilated suspension surface looks like come from extensional flows. Smith showed images of surface roughening for suspensions under extension for a high strain rate, contrasting with a lower strain rate where no such surface change was observed [18]. A followup to these extensional experiments reported that surface roughening was observed after the force started to increase but before peak force was reached [19]. We note that many of these images show shear jamming after flow has stopped rather than surface roughening during a steady shear, and while shear jamming is often found to occur in DST suspensions [20], it is not equivalent to DST [21]. Impact experiments have also shown roughened surfaces as a result of dilation [22,23]. It is perhaps suspicious that the best images of surface roughening are from extension and impact experiments. While there are some similarities between shear thickening in steady-state shear and transient extensional flows, there are also significant differences; for example, transient extensional flows can result in stresses orders of magnitude larger than steady-state shear [24,25]. It remains an open question whether observations of surface roughening in extensional flows apply straightforwardly to shear flows.

While DST is described by a steady-state averaged apparent viscosity curve, time-resolved measurements reveal that both shear and normal stresses fluctuate, sometimes by orders of magnitude [26,27]. Despite the strong fluctuations, there remains a proportionality between shear and normal stresses with a coefficient of order 1, suggestive of a Coulomb frictional relationship between stresses [2,26,27]. DST in the time-averaged apparent viscosity curve can be attributed to the contribution of fluctuations to the high-stress state, while a low-stress state follows the trend of an apparent viscosity curve without shear thickening [26]. Stress fluctuations [28,29] and density and shear rate fluctuations [30–32] have also been found to occur in localized regions, rather than be uniform throughout the suspension. If dilation is related to stresses [2], then the fluctuations and localization of stresses should have a connection to surface roughening, but no such fluctuations or localization in surface roughening have ever been reported in steady-state flows.

In this work, we present images and video of the surface of DST suspensions along with simultaneous rheology measurements under steady shear. We focus on images at the surface because it is the surface roughening that is predicted to more directly affect the macroscopic behavior through changes in the normal stress from surface tension [2], as opposed to changes in the bulk packing fraction. Specific issues we address are (1) to present clear video and images of surface roughening under steady shear, (2) show whether surface roughening (and thus dilation) occurs in the same stress range as DST, and (3) determine whether surface roughening is localized and fluctuates along with stresses.

The remainder of the paper is organized as follows. Section II describes the apparatus, materials, and rheometer measurement procedure. Section III shows images of surface roughening and describes observations of intermittency and localization. An explanation of image analysis methods to quantitatively track surface roughening over time from the video is given in the Appendix. Section IV A shows simultaneous time series of stress and surface roughening measurements to identify their relationship during fluctuations. Section IV B presents statistics on the probability of surface roughening under different conditions such as at high- and low-stress states. Sections IV C and IV D present measurements over a range of shear stress and stresses to confirm that surface roughening occurs at stresses and shear rates in the shear thickening range and above. Section V presents some interpretation of the data, discusses some of the consequences of a macroscopic behavior dependent on boundary stiffness rather than bulk properties alone, and summarizes our understanding of the role of dilation in the high-stress state of DST.

II. MATERIALS AND METHODS

A. Materials

We used cornstarch and water as an example of a typical DST fluid [1]. Cornstarch was purchased from Argo and suspended in tap water near room temperature. The suspensions were mixed and measured at a room temperature of 22.0 ± 0.6 °C and humidity of 48 ± 6%, where the uncertain-

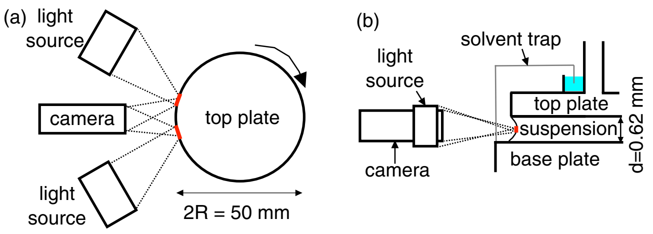

FIG. 1. Illustration of the experimental setup (not to scale). (a) Top view. (b) Side view. The suspension is sheared underneath the rheometer top plate. Dotted lines illustrate paths of light rays from the edges of the light source to the edges of the camera sensor. The camera views direct reflections as bright spots (red) on the suspension surface. When the suspension dilates, the roughened surface produces a diffuse reflection over a wider area of the suspension surface.

ties represent day-to-day variations in the respective values. A four-point scale was used to measure quantities of cornstarch and water to obtain a weight fraction ϕ_{wt}. Each suspension was mixed until no dry powder was observed. The suspension was further shaken in a Vortex Genie 2 for approximately 30 s on approximately 60% of its maximum power output.

Packing fractions of cornstarch suspensions are difficult to compare, mainly due to the different adsorption of water into nominally dry cornstarch at different temperature and humidity levels [33]. For comparison to data from other researchers in the DST range, we use an effective packing fraction scale ϕ_{eff} that is based on the measured shear rate $\dot{\gamma}_c$ at the onset of DST. This is more precise in reproducing data than comparing values based on measured weight fractions in different environmental conditions for packing fractions in the DST range, due to the divergence of suspension properties near the liquid-solid transition at ϕ_c [33]. We use the effective packing fraction $\phi_{\text{eff}}/\phi_c = 1 - 0.0475\dot{\gamma}_c^{0.268}/d$, where d is the rheometer gap in units of mm and $\dot{\gamma}_c$ is in units of s^{-1}, which was obtained previously by fitting $\dot{\gamma}_c$ as a function of ϕ and d in the range 0.61 mm $\leqslant d \leqslant$ 1.8 mm [33]. We obtain ϕ_{eff} for our data by inputting into this equation measurements of $\dot{\gamma}_c$, d, and a measurement of ϕ_c under current environmental conditions [33].

B. Apparatus

Experiments involved a combination of rheological measurements with high-speed video of the suspension surface, as illustrated in Fig. 1. Rheological measurements were performed with an Anton Paar MCR 302 rheometer with a suspension placed between parallel plates. The rheometer measured the torque M on the top plate and angular rotation rate ω of the top plate. In different experiments, either torque or rotation rate could be controlled, while the other was measured as a response. The spatially averaged shear stress is given by $\tau = 2M/\pi R^3$, where R is the radius of the top plate. The spatially averaged shear rate at the outer radius of the plate is used as a reference parameter, which is given by $\dot{\gamma} = R\omega/d$, where d is the rheometer gap between the top and base plates (i.e., the height of the suspension). Note that these parameters τ and $\dot{\gamma}$ measured by a rheometer represent macroscopically averaged values of shear stress and shear rate rather than a local constitutive relation. The apparent viscosity—corresponding to a spatially and time-averaged macroscopic viscosity measured in a rheometer—is reported as $\eta = \tau/\dot{\gamma}$ in a steady-state average. We also measured the force F on the top plate of the rheometer (upward positive) and report the spatially averaged normal stress $\sigma = F/(\pi R^2)$ with a resolution of 2.5 N. To calibrate the normal stress, we subtract the normal stress on the suspension at rest, which is due to surface tension at the liquid-air interface.

Since our measurements involved imaging of the suspension-air interface, special consideration was given to how the placement of the suspension affects the imaging of the suspension-air interface. In steady shear experiments, there is a tendency for the side surface of the suspension to become unstable, in particular, blobs or granules of suspension build up on the side and protrude outward temporarily [34], interfering with imaging of the surface. We found this effect was minimized if the suspension did not extend all the way out to the edge of the plate, as shown in Fig. 1(b), which presumably confines the suspension in place better by providing more surface area on the parallel plate surfaces for the contact line of the liquid-air interface. Therefore, when loading the suspension we adjusted the top plate height so the suspension had a mean radius of 24.75 ± 0.25 mm, compared to the top plate radius of $R = 25.00$ mm. This results in up to a 6% underestimate in shear stress τ and up to a 4% underestimate in normal stress when the plate radius R is used in calculations. The resulting range of rheometer gaps was typically $d = 0.62 \pm 0.02$ mm, where the ± corresponds to the standard deviation of different experiments, unless otherwise noted. Note that surface roughening is a robust phenomenon, visible by eye for different sample radii and the wide variety of other measuring conditions where we observe DST, and the precautions taken here are just to obtain clear images with a camera that are easy to analyze without other phenomena getting in the way.

The camera and lights were arranged as shown in Fig. 1 to visualize the side of the suspension. High-resolution images, videos, and examples shown in Secs. III, A, and IV D were taken with a digital single-lens reflex (DSLR) camera with a micro lens. A small amount (<0.1%) of powdered graphite was added to suspensions to visualize shear for high-resolution images and video. High time resolution measurements for comparing the timing of stress fluctuations with surface roughening reported in Secs. IV A–IV C were taken with a Phantom Miro M110 camera with a micro lens. One or two light sources were placed at angles such that direct reflection from the suspension surface would be observed at the camera. Such direct reflection was found to produce the highest contrast between the shiny surface at rest and a rough surface with a diffuse reflection when the suspension dilates. The angles of the light sources were also set to produce relatively large bright spots to increase the fraction of surface observed. For quantitative measurements in Sec. IV B, these bright spots were 5 mm long and separated by 7.5 mm. The resolution was 20 pixels across the rheometer gap d and 640 pixels in the horizontal direction. This viewed about 12% of the suspension surface, although only about 6% of the circumference of the surface was reflecting bright spots. Video data were recorded as 8-bit grayscale images.

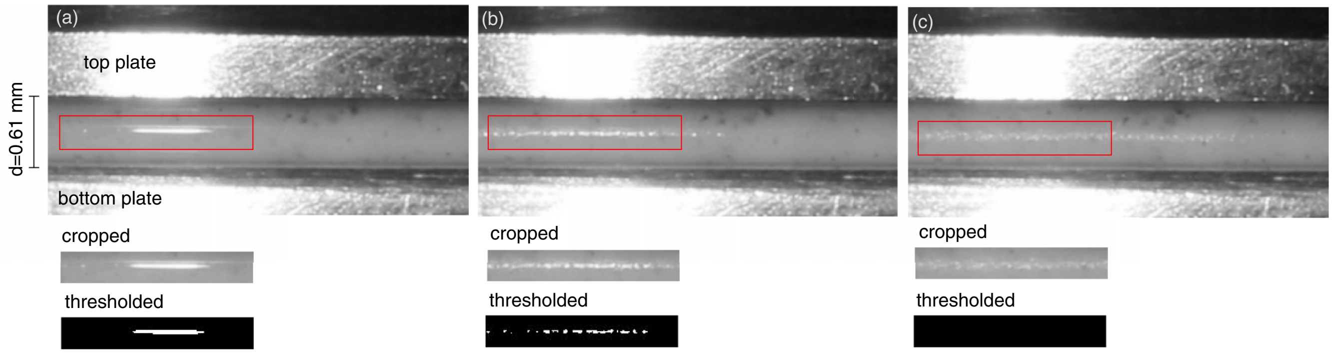

FIG. 2. Side view of the suspension in the rheometer. (a) A suspension at rest with no surface roughening, indicated by the shiny surface. (b) A suspension under shear with a growing region of surface roughening, an indicator of overall dilation. Surface roughening is indicated by the speckled pattern, due to the rough surface reflecting light diffusively. (c) A suspension with a maximally roughened surface under shear. Lower images illustrate the cropping and thresholding used to identify the presence of surface roughening based on counts of the number of bright pixels. The red boxes in the top images outline the cropped region.

A solvent trap [shown in Fig. 1(b)] was placed around the suspension to minimize moisture exchange between the suspension and the room atmosphere. The solvent trap is a box that surrounds the sample but is not in contact with the sample. It has a lipped lid touching water contained in a cup on the top plate so that the atmosphere inside the trap is separated from the room atmosphere by a water barrier. This was specially designed with a square horizontal cross section made of transparent acrylic to avoid distortion of the images from light passing through the walls of the liquid trap.

The lights used for taking video heated up the suspension during measurements, and the custom solvent trap required a base that interfered with the rheometer temperature control, resulting in suspension temperatures in the range 23.3 ± 1.7° C for different experiments, measured at the rheometer plate.

C. Measurement procedure

A preshear was used to eliminate effects of loading history on the suspension to produce steady-state measurements. The preshear consisted of a linear ramp in shear rate or stress from rest to a value above the shear thickening range, lasting at least 200 s. Steady-state measurements started immediately after this, at the same shear rate or stress the preshear ended at to minimize acceleration.

The first and last measurements on each suspension were viscosity curves, which were used to identify the shear thickening range and confirm reversibility and a lack of time dependence of the sample. The critical shear rate $\dot{\gamma}_c$ and shear stress τ_c are defined to be at the onset of DST, obtained at the lowest shear rate $\dot{\gamma}$ where $\partial\eta/\partial\dot{\gamma} > 1$ [33]. Since we generally observe the shear thickening range is followed by a shear thinning range at higher shear rates [2], to identify the upper end of the shear thickening range we define the shear rate $\dot{\gamma}_{\max}$ and shear stress $\tau_{\max}$ as their maximum values in the shear thickening range, i.e., at the local maximum of viscosity.

Viscosity curves were measured with a controlled shear rate, and the ramp was done at a rate of 300 to 1000 s per decade. Each ramp was immediately remeasured in reverse order to confirm there was no hysteresis or time-dependent effects. With the last measurement being a repeat of the viscosity curves, we checked the magnitude of any time-dependent effects such as evaporation over the course of measurements. Over the course of our longest series of experiments of 4 h, the measured value of $\dot{\gamma}_c$ decreased by 30%, corresponding to an increase of up to 0.008 in ϕ_{eff}/ϕ_c in the DST range.

The relative timing of the video and stress measurements was done manually by triggering the video after the steady state is reached in rheometer measurements. This is referred to as time $t = 0$ in both measurements. This process results in an uncertainty of about 1 s in the relative time between the two measurements reported in Secs. IV A and IV B.

III. OBSERVATIONS OF SURFACE ROUGHENING

An example video of the suspension surface is shown in Supplemental Video 1 [35] for an applied shear stress $\tau = 200$ Pa (in the middle of the shear thickening range) and effective packing fraction $\phi_{\text{eff}}/\phi_c = 0.95$ (in the middle of the packing fraction range with DST), played back at 20× real speed. Snapshots of different behaviors are also shown in Fig. 2. We focus our attention on the reflection of light from the surface of the suspension, as that is closely related to deformation of the liquid-air interface, which is predicted to be the relevant consequence of dilation. For a suspension at rest, and much of the time during steady shear, there is a thin bright strip of light reflected off the surface, as illustrated in Fig. 2(a). This is the direct reflection of the light from the source off of a smooth, shiny surface. The bright spot is a thin strip even though the light source is circular because the resting liquid-air interface is highly curved in the vertical direction due to surface tension and less curved in the horizontal direction due to the plate curvature, as illustrated in Fig. 1. During shear, the bright spot can fluctuate in size, shape, and position somewhat due to slight deformations of the surface. These fluctuations may be due to vibrations of the experimental apparatus.

The effects of dilation on a suspension during shear can be observed in Figs. 2(b) and 2(c) and Supplemental Video 1 [35]. Instead of a single bright spot, the surface now appears speckled over a wider area. The change in the reflection of light indicates a deformation of the surface of the suspension. More specifically, this can be understood as a consequence of dilation according to the following argument. When a dense suspension is sheared and dilates, particles poke through the liquid-air interface, while liquid from the surface migrates into the interstices between particles in the bulk. Since the average particle diameter of 14 μm is too small to see individual particles but larger than the wavelength of light, the direct lighting reflects diffusively off the roughened surface, resulting in the speckling seen in Figs. 2(b) and 2(c). The surface appears progressively rougher and dimmer because there is less direct reflection. The region where reflected light is coming from also spreads out horizontally and vertically because the roughened surface results in additional localized direct reflections from the light source to the camera where there were none before. A larger, dimmer speckled region indicates a larger surface deformation to reflect light at wider camera angles.

Shear can be observed everywhere and at all times on the surface without dramatic variations in shear rate, for example, in Supplemental Videos 1 and 2 [35] in the relative motion of the black tracer particles. This confirms that that neither observations of surface roughening nor DST reported here correspond to statically jammed states, shear banding, or other transitions in shear profiles.

FIG. 3. A series of images of the suspension at different times separated by 0.033 s, showing the propagation of a localized region of surface roughening (the faint speckled pattern) past the bright spot from left to right.

A. Intermittency

Supplemental Video 1 [35] shows intermittent changes in the surface reflection. Specifically, we occasionally observe surface roughening events where the images transition from the bright spot seen in Fig. 2(a) into the speckled surface roughening pattern shown in Fig. 2(b) on the way to the dimmer speckled pattern in Fig. 2(c), before brightening again and reverting back to a undeformed surface.

B. Localization and propagation

Supplemental Video 2 [35] shows examples of localized surface roughening; i.e., surface roughening does not have to span the entire system at once, and it can grow or propagate over time. These data were taken at a constant shear stress of $\tau = 100$ Pa and $\phi_{\text{eff}}/\phi_c = 0.90$ (at the low end of the packing fraction range of DST) where these localized events are more apparent, and the video is played back at 4× real speed. A series of images in Fig. 3 shows an example of localized roughened surface propagating past a bright spot, although the series of images is not nearly as clear as the video. The series of images shows a surface roughening event first appearing to the left (downstream) of the bright spot, and propagating to the right (upstream). Such propagation events are numerous, but are more frequent at higher stress. From the video, it can be seen that the fronts propagate at a constant speed, faster than the plate speed. Regions with surface roughening propagate in both directions, although the majority propagate in the direction opposite the top plate rotation. This is reminiscent of measurements of localized high-stress regions found to propagate through the interior in stress-controlled measurements [29], where the intermittent and localized stress fluctuations occur near the outer radius of the plate and propagate in both directions (i.e., with and against the flow). These fluctuations are distinct from previously observed density waves which are periodic rather than intermittent [31,32],

Although not all regions of surface roughening are the same size, it appears that they all have a characteristic size at a given packing fraction and shear rate. Our preliminary investigations into lower packing fractions $\phi_{wt}/\phi_c \leqslant 0.89$ in the continuous shear thickening (CST) range (defined by viscosities that increase with shear rate, but less steeply than DST [33]) resulted in smaller regions of surface roughening, often smaller than the bright spot in our images. However, the instability of those suspensions at high stress limited us to measuring at lower stress and prevented us from collecting systematic packing-fraction-dependent statistics to compare to the higher stresses reported here. With small regions of surface roughening and two bright spots, we occasionally observe two separate surface roughening events at the same time (a few percent of events), so there can be more than one surface roughening event occurring at once, and there may be even more on other portions of the surface that are not in our viewing range. In contrast, the surface roughening events in Supplemental Video 1 [35] do not have a clear propagation direction but rather appear to span our measurement region. This may correspond to a limit where regions with surface roughening are significantly larger than the measurement region and with growth rates that are faster than we can resolve, perhaps due to the higher packing fraction of that data.

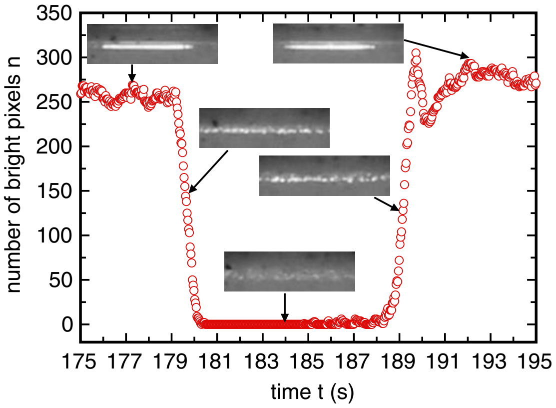

FIG. 4. Number of bright pixels n as a function of time for a single surface roughening event, showing the corresponding raw images in the experiment. The low values of n correspond to when surface roughening is observed.

C. Using a reduction in direct reflection as a quantitative proxy for surface roughness

We identify a quantitative measure of surface roughening from images so that we can calculate statistics and compare time series to those of stresses later. Because the bright spot is a result of direct reflection off a nearly flat surface, we found that the absence (or a smaller number) of bright pixels is a good proxy for surface roughening and thus dilation. We show an example time series of the number of bright pixels n in the region around where the direct reflection occurs for a typical surface roughening event in Fig. 4 for a controlled shear stress $\tau = 200$ Pa at $\phi_{\mathrm{eff}}/\phi_c = 0.945$, in the DST range. Cropped snapshots of the surface are shown at a few points in time. Initially, when n is high, the snapshot shows a single bright spot, indicating a smooth surface, similar to Fig. 2(a). There is a distinct surface roughening event where the number of bright pixels drops rapidly to near zero for a while, before returning to its high value. When n is at intermediate values, the snapshots show speckled patterns due to a partially rough surface, similar to Fig. 2(b). When $n = 0$, the snapshot shows only dim, diffuse reflection corresponding to a rougher surface, similar to Fig. 2(c). We manually checked that each surface roughening event that we could see in a video resulted in a small n, while n remained large when surface roughening was not seen in videos. This confirms that surface roughening events can be distinctly tracked based on the number of bright pixels as a function of time. Details of how we define the number of bright pixels, obtain the threshold number of pixels to identify dilation, and verify their robustness are found in the Appendix.

IV. CORRELATION BETWEEN SHEAR RATE FLUCTUATIONS AND OBSERVATIONS OF SURFACE ROUGHENING

A. Time series of stress measurements and surface reflections

The relation between surface roughening and stress fluctuations is shown in a time series of the number of bright pixels along with simultaneous stress measurements. Figure 5 shows data for $\phi_{\mathrm{eff}}/\phi_c = 0.952$, in the DST range, and at a controlled shear rate $\dot{\gamma} = 0.2\ \mathrm{s}^{-1} \approx 1.2\dot{\gamma}_{\max}$, so that the mean stress corresponds to the high-stress state of DST. For these statistics, we use two light sources to generate two bright spots. Bright spot analysis is done separately for each observation location, and we report time series for the number of bright pixels n_L for the left (downstream) spot and n_R for the right (upstream) spot. Several stress drop and increase events can be observed as the stresses fluctuate between the low- and high-stress states of DST. For each stress drop and increase, the normal and shear stress tend to track each other fairly well. Each time the stresses drop to near zero, a few seconds before there is a simultaneous sharp increase in both n_L and n_R from zero up to near the smooth surface value n_p (indicated by the vertical dashed lines in Fig. 5). This indicates that the end of surface roughening occurs within a few seconds of the large stress drops (although the normal stress tends to increase slightly before the large drop). On the other hand, each time the stresses start to increase from near zero toward their mean values, both n_L and n_R drop to zero within a few seconds of the start of the stress increase (these times are marked by the large open circles in Fig. 5). This indicates that stress increases tend to occur along with surface roughening. Together, these observations indicate a strong correlation between surface roughening and the high-stress state of DST suspensions.

While we tend to see surface roughening occur along with high stresses in Fig. 5, there are also many instances where surface roughening disappears (either n_L or n_R increases) while the stresses remain high, although in these cases the disappearance of surface roughening is not usually simultaneous at both measuring locations. Since we only observe a small

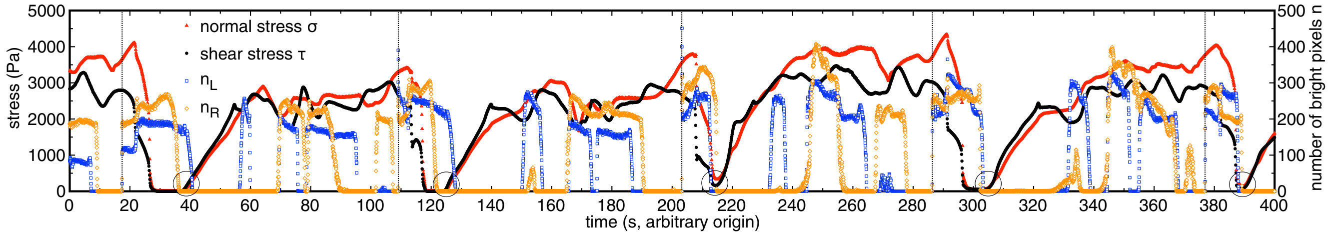

FIG. 5. A time series showing the relation between surface roughening and stress. Left axis: shear stress τ (solid circles) and normal stress σ (solid triangles). Right axis: number of bright pixels in each bright spot, n_L (open squares) and n_R (open diamonds). The start of stress growth events are indicated by large open circles. Both n_L and n_R drop to zero within a few seconds of each of these events, indicating the stress increases occur along with surface roughening. Vertical dashed lines: Times where both n_L and n_R increase simultaneously, a few seconds before both stresses drop to near zero, indicating that stress drops occur along with the end of surface roughening.

TABLE I. Probabilities of surface roughening at single-point measurements p_1, and simultaneously at two-point measurements p_2, compared for different shear stress conditions as explained in the text. Surface roughening is common at the high-stress state and uncommon in the low-stress state. No surface roughening is found at times when both the stress and stress growth remain low for the following 9 s. Surface roughening is most common during stress growth periods that transition from the low-stress state to the high-stress state and is always found after consistent stress growth for 9 s. The correlation length λ for regions of surface roughening is extrapolated from these probabilities. The extrapolation suggests that the size of regions of surface roughening during the stress growth period typically spans the surface of circumference 157 mm.

	p_1	p_2	Length λ
High stress (>1400 Pa)	52%	40%	46 mm
Stress growth	90%	86%	240 mm
Stress growth for previous 9 s	100%	100%	∞
Stress drop	7%	3%	9 mm
Low stress (<460 Pa)	21%	11%	15 mm
Low stress, low growth	12%	6%	14 mm
Low stress, low growth for next 9 s	0%	0%	NA
CST (low stress)	4%	0.08%	−1 mm

fraction of the surface, we likely miss a number of surface roughening events, which may exist elsewhere on the surface in the remaining portions of the high-stress periods. In contrast, while the stress remains low, we observe a complete lack of surface roughening events, except when they are within a few seconds of a stress increase. These observations are at least consistent with the hypothesis that the high-stress states require surface roughening somewhere on the surface.

The drops in n_L and n_R do not coincide as well with each other near the time of stress increase as they do near the time of stress drops, suggesting that when a stress drop occurs, regions of surface roughening shrink rapidly, while during stress increases, a longer time is required for surface roughening to propagate around the suspension. The growth in stress to the high-stress state also tends to be slower than the drop in stress to the low-stress state.

B. Statistics relating surface roughening and stress

To collect more statistics on surface roughening events, we measured stresses and surface roughening with longer time series for six different suspensions. Three of the suspensions measured correspond to packing fractions in the DST range ($\phi_{\text{eff}}/\phi_c = 0.952, 0.953, 0.957$), with applied shear rates $\dot{\gamma} \approx 1.2\dot{\gamma}_{\max}$, where the mean stress is close to the high-stress state. We calculated the probabilities of surface roughening occurring at each bright spot p_1 under different conditions to quantify the likelihood of surface roughening in different states such as the high-stress or low-stress states. The following numbers in this subsection are averaged (weighted by time step) over the three data sets in the DST range where we observed a high-stress state. Probabilities of surface roughening p_1 are summarized in Table I.

In the high-stress state $p_1 = 52\%$, where the high-stress state is defined as when the shear stress $\tau > 1400$ Pa, just outside of the range of fluctuations observed in the high-stress state in Fig. 5. In contrast, in the low-stress state $p_1 = 21\%$, defined initially as when $\tau < 460$ Pa (25% of the mean stress). While the stress usually drops much lower, as low as the stress $\tau_c = 2 \pm 1$ Pa at the onset of DST [26], it does not always reach that low level, so the stress thresholds for counting events are higher to include all significant stress drop events in our data. These statistics indicate that surface roughening is significantly more likely in the high-stress state than in the low-stress state.

We refine the above statistics by identifying distinct transitions between the high- and low-stress states and further subdividing the time series to include stress drop and stress growth periods. Each transition to the low-stress state is defined to occur when the shear stress drops below 460 Pa, and the transition back to the high-stress state is defined when the shear stress next exceeds 1400 Pa. Successive transitions to the same stress state are not counted until a transition to the other stress state, and the thresholds are set at different values to avoid counting extra events due to jitter of the time signal around the thresholds. With this counting, we find a total of 50 such pairs of stress transition events and 537 surface roughening events among the three time series that reach the high-stress state.

We identify the stress growth period corresponding to the transition from the low-stress state to the high-stress state, defined as when the shear stress is in between the thresholds of 460 and 1400 Pa, and the five-point slope of shear stress over time is greater than 50 Pa/s (the mean slope seen in the stress growth regions of Fig. 5 is found to be 150 Pa/s for each data set). During this stress growth period $p_1 = 90\%$. These probabilities of surface roughening are even higher than those in the high-stress state, indicating that surface roughening is correlated more strongly with stress growth than the high-stress state.

The probability of surface roughening in the growth period increases to $p_1 = 100\%$ when we only include data where the stress growth exceeded 50 Pa/s for the preceding 9 s (this limited range of data still includes 1800 data points from 23 distinct stress growth periods). The stress growth period required for $p_1 = 100\%$ may correspond to the maximum time it takes for a region of surface roughening to grow and span the entire surface to ensure that we observe surface roughening at both measuring locations. Since the average time required to grow up to the mean stress of the high-stress state of 2460 Pa is 16 s, this means that surface roughening would consistently span the entire surface by the time the high-stress state is reached by sustained typical growth from the low-stress state.

Given the high correlation observed between surface roughening and stress growth, we narrow the definition of the low-stress state to times when the shear stress is below the threshold of 460 Pa and the slope of stress over time is less than 50 Pa/s. The probability of surface roughening in this period with low stress and low growth in stress is $p_1 = 12\%$. This is more distinct from the high-stress state and suggests the surface roughening observed at low stress is probably more associated with the growth in stress over time.

If we further limit our analysis of statistics in the low-stress state to data points that satisfy the criteria for low stress and low growth in stress for the following 9 s, then we find no surface roughening ($p_1 = 0$). This smaller range of data with no surface roughening still includes 8000 data points. While 9 s is the longest persistence time required, the persistence time at low stress is usually much shorter; for example, for a persistence time of 2 s, p_1 drops to half of its value with no persistence time. Since the surface roughening occurs at the end of low-stress periods followed by stress growth, this time corresponds to the longest time it takes for the stress growth at the plates to respond to surface roughening.

We finally consider statistics of surface roughening during the stress drop period that transitions from the high-stress state to the low-stress state. We find surface roughening $p_1 = 7\%$ when the stress is in between the low-stress and high-stress thresholds and has a slope of less than -1000 Pa/s. For all such events, there is a time within the 3 s before the identified stress drop threshold where no surface roughening is observed during that period. Since the stress drops typically last less than 1 s—comparable to the relative timing error—we cannot calculate statistics for extended time periods of stress drop. This indicates a correspondence between the stress drop and a lack of surface roughening, similar to the low-stress state.

1. Size of regions of surface roughening

While we observe surface roughening at a single point on the surface in the high-stress state $p_1 = 52\%$ of the time, it is reasonable to ask if surface roughening at some point on the surface is required at all times to maintain the high-stress state. Mechanically, it that would be required of a model in which the measured shear stress comes from friction transmitted through contact networks, in which the normal force is limited by surface tension at the liquid-air interface [2].

We infer a typical size of the region of surface roughening by comparing the probability p_1 of surface roughening at a single point with the probability p_2 of surface roughening simultaneously at both observation points on the surface. Probabilities of p_1 and p_2 are shown in Table I for the different stress conditions. p_2 is even more distinct between different stress conditions shown in the table than p_1, suggesting the size of regions of surface roughening may be a significant factor in determining stress states.

If we assume the regions of surface roughening have a distribution of sizes characterized by a correlation length λ and surface roughening events appear in the observation region one at a time, the probability of finding surface roughening at different spots of size $L = 5$ mm separated by a distance $s = 7.5$ mm at the same time can be estimated as

$$\frac{p_2}{p_1} = \exp\left(-\frac{s+L}{\lambda+L}\right). \tag{1}$$

Rearranging Eq. (1) yields the correlation length λ, which is shown in Table I for different stress conditions. In the stress growth state, the extrapolated correlation length of 240 mm is larger than the circumference of 157 mm, suggesting that the size of regions of surface roughening during the stress growth period is likely to cover much of if not the entire surface. This is consistent with the conclusion that the stress growth period typically results in surface-spanning surface roughening. On the other hand, the extrapolated correlation length in the high-stress state is only 29% of the circumference. This is consistent with the observation that we do not always observe surface roughening during the high-stress state, and it suggests a single surface roughening event may only be covering an average of 29% of the surface in the high-stress state. The fact that we observe $p_1 = 52\% > 29\%$ in the high-stress state suggests that either the distribution of surface roughening event sizes is not well represented by a typical correlation length as expressed in Eq. (1), or there is an average of more than one surface roughening event at a time on the surface in the high-stress state. Indeed, measurements of local stress typically found two high-stress regions at a time [29]. While we cannot guarantee with our limited observation locations that there is always surface roughening at some point of the surface in the high-stress state, the two-point statistics are consistent with that hypothesis for a reasonable assumption of how surface roughening events at two measuring points are correlated.

2. Data sets with no high-stress state

Three of the packing fractions we measured statistics at were in the CST range, although due to instabilities at the surface, we could not take long measurements above $\tau_{\max}$. Instead, we took measurements at shear rates within the shear thickening transition ($\dot{\gamma}_c < \dot{\gamma} < \dot{\gamma}_{\max}$). Since these measurements were at both lower packing fractions and lower relative shear rates than the measurements where the high-stress state was observed, we cannot draw systematic conclusions regarding the difference in surface roughening between CST and DST at this time, but we can still test the relation between surface roughening and stresses. At $\phi_{wt}/\phi_c = 0.84$ and shear rate $\dot{\gamma} = 125\ \mathrm{s}^{-1}$, no surface roughening events were observed over 145 s, and the shear stress did not fluctuate much above its mean of 40 Pa (this is well into the DST stress range which starts at $\tau_c = 2 \pm 1$ Pa for all packing fractions). In the other two data sets at $\phi_{wt}/\phi_c = 0.85$, $\dot{\gamma} = 75\ \mathrm{s}^{-1}$ and $\phi_{wt}/\phi_c = 0.89$, $\dot{\gamma} = 20\ \mathrm{s}^{-1}$, we observed 2078 surface deformation events where part of the bright spot dimmed with $p_1 = 4\%$, but no stress fluctuations much larger than their respective averages of 27 and 28 Pa. While there are numerous surface deformation events in these cases, they are brief, so the probability p_1 is small. The probability of both bright spots dimming at the same time drops to $p_2 = 0.08\%$, corresponding to a nearly zero correlation length according to Eq. (1). These probabilities suggest very localized surface deformation events—indeed in many cases we observe dimmed regions to be smaller than the bright spots used for measurement regions. Thus, while surface deformation events can occur in flows that do not reach the high-stress state, these events are too small or brief to produce the surface-spanning surface roughening required for stress growth to reach the high-stress state.

C. Viscosity curves with surface roughening

The relation between surface roughening and shear thickening was measured in a viscosity curve at $\phi_{wt}/\phi_c = 0.94 \pm 0.06$ and rheometer gap $d = 0.495$ mm [36]. Measurements of shear stress τ, normal stress σ, and the number of bright pixels n are shown as a function of shear rate in Fig. 6. Stresses are reported every second, and the number of bright pixels

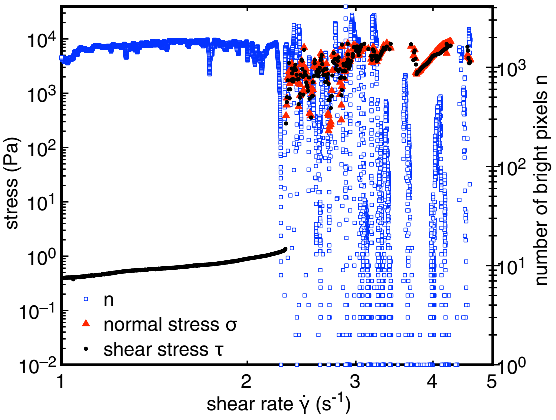

FIG. 6. A viscosity curve showing shear and normal stress (left axis) and number of bright pixels n on the surface (right axis), as a function of shear rate $\dot{\gamma}$. The high-stress range coincides with the range of intermittent surface roughening events.

is reported 24 times per second so that fluctuations can be seen. There are some gaps in the stress data where the shear rate left steady state because the stress reached the limit of what the rheometer could provide. The sharp jump in stresses identifies DST with a clear distinction between the high- and low-stress states. In the high-stress range at high shear rates, the normal and shear stress remain strongly coupled [27], and there are large fluctuations in the number of bright pixels to low values, indicating intermittent surface roughening. Note that the short-timescale stress fluctuations are less visible than in Fig. 5 due to the longer averaging time of the stress data. At shear rates below the shear thickening transition, there are no fluctuations in the number of bright pixels, and a complete lack of surface roughening is observed. This confirms that the intermittent surface roughening occurs only in the high-stress range and not at the low-stress range of the viscosity curve.

We repeated this experiment four times with ramps of both decreasing and increasing shear rate and at two different packing fractions; in each case, surface roughening was observed only in the high-stress state, and the transition between intermittent surface roughening and no surface roughening happened within a few seconds of crossing the shear thickening transition.

These large fluctuations in shear and normal stress by several orders of magnitude between low- and high-stress states of DST are similar to previously reported large stress fluctuations which are the dominant contribution to the high-stress state of DST [26,27]. These intermittent fluctuations in stress by orders of magnitude are distinct from periodic density waves that are predicted to occur based on the Wyart-Cates model only in the shear thickening transition under applied stress, where shear rate fluctuations are around 5–z10% [30–32].

D. Surface roughening probability as a function of applied shear stress

Since the DST transition is sharp in shear rate, there is not much opportunity to observe how surface roughening evolves in the shear thickening range from that perspective.

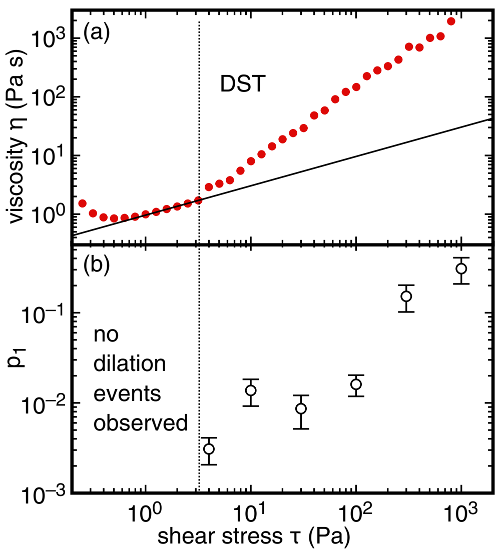

FIG. 7. (a) A viscosity curve $\eta(\tau)$. Solid line: line of slope 1/2 used to determine the onset of DST. Vertical line: $\tau = \tau_c$, corresponding to the onset of DST. (b) The probability of surface roughening p_1 as a function of controlled shear stress τ. Surface roughening is found only for $\tau > \tau_c$, and the probability of surface roughening increases with stress in the shear thickening range.

On the other hand, the shear thickening transition exists over a nonzero range of stress in stress-controlled measurements. In this subsection, we report statistics as a function of shear stress in stress-controlled measurements at a fixed packing fraction to observe the evolution of surface roughening through the shear thickening range.

To identify the stress range of shear thickening, a viscosity curve from stress-controlled measurements is shown in Fig. 7(a) for $\phi_{\text{eff}}/\phi_c = 0.91$ (at the low end of the range of packing fractions with DST). While $\eta(\dot{\gamma})$ has a discontinuous jump at this packing fraction [33], DST in stress controlled measurements is characterized by slopes of $\log \eta(\tau)$ approaching 1 in the limit as ϕ_{eff} approaches ϕ_c [37,38]. For purposes of distinguishing DST in stress-controlled measurements from other shear thickening, we identify the onset of DST as the lowest stress value where the local value of $\partial\eta/\partial\tau$ exceeds 1/2 [2]. DST is found for $\tau > \tau_c = 3$ Pa, indicated by the vertical dashed line in Fig. 7.

The probability of surface roughening p_1 is shown for constant applied stress measurements in Fig. 7(b) for similarly prepared suspensions as that shown in Fig. 7(a) (with a variation of ϕ_{eff}/ϕ_c up to 0.008 based on measurements of $\dot{\gamma}_c$). The plotted errors include the Poisson error assuming distinct (i.e., noncontinuous) surface roughening events are independent, plus a fractional error of 18% due to the small variation in ϕ_{eff}/ϕ_c, which is calculated from an extrapolation of a comparison of the probability of surface roughening for the different time series reported in Table I. For $\tau = 1$ Pa ($<\tau_c$), where there is no shear thickening, we find zero surface roughening events. For comparison of statistics, this measurement was made over the same time period that 44 surface roughening events were observed at $\tau = 4$ Pa ($>\tau_c$). For reference, the distributions $p(n/n_p)$ are shown in Fig. 9

of the Appendix for $\tau = 1$ and $\tau = 1000$ Pa. For $\tau > \tau_c$, the probability of surface roughening typically increases with τ, indicating another correlation between surface roughening and higher stress in the shear thickening range. We find the increasing probability of surface roughening with increasing stress in the shear thickening range tends to correspond to longer lived surface roughening events, with no clear trend in the frequency of events observed at a single point. The frequency of events observed at a single point depends on both the correlation length and frequency of surface roughening events. Since a correlation length for stress fluctuations was found to decrease with increasing stress [17], it may be that the frequency of surface roughening events increase with stress as well. These results confirm that surface roughening occurs in the same stress range as DST (where $\tau > \tau_c$), but surface roughening is not found at lower τ.

V. DISCUSSION

A. Stress growth and failure

The repeated growth of stress to a plateau with fluctuations seen in Fig. 5 is reminiscent of stress-strain curves of other disordered granular materials and soils that dilate. In such systems, the plateau represents the ultimate strength of the material, and fluctuations around a plateau are characteristic of a failure regime, where drops in stress correspond to localized failures. Such cycles of stress growth and failure around the steady-state stress have been observed in local stress measurements of a DST suspension [29]. Such localized failures have been observed as system-spanning force networks that repeatedly form and break up in the steady state in simulations of DST suspensions [3,39]. The observation that surface roughening covers a significant fraction of the surface in this high-stress state is consistent with a picture in which the dilated surface provides the normal force to transmit stress along these localized structures. Strains of order 1 are have been observed before for such failures in dense suspensions [13], and the stress growth rate observed in Fig. 5 and our other data sets indicates that it typically takes a strain of 3.5 ± 0.5 to reach the failure stress plateau, on the expected order. In contrast, during stress growth up to this plateau stress, we infer from Table I that surface roughening tends to cover the entire surface by the end of the stress growth regime, more than in the high-stress plateau. Since the stress is still growing, this suggests the force network has not yet reached a point of failure, remains connected, and does not start to fail locally until the stress plateau is reached.

The drop in stress from the high-stress state down to the low-stress state that we observe in Fig. 5 is a feature that is not typically observed in stress-strain curves of disordered granular materials and soils. This indicates that the structure formed in the high-stress of DST state fails completely to support any stress on occasion and reverts to a fluid-like state. It is possible for this melting to occur, and for the particles to rearrange and start the process of stress growth over again because this is a closed system. However, the possibility and even likelihood that the structures fail completely indicates that the structures formed in DST suspensions are much more fragile than a dry granular material or soil, which do not suffer such complete failures in a similar shear.

B. Transition time and the pore flow rate

We observed a transition time between high- and low-stress states. Specifically, a complete lack of surface roughening is observed in the low-stress state when there is not rapid stress increase within the following 9 s (Table I). Likewise, surface roughening is observed 100% of the time following 9 s of persistent stress growth (Table I). This 9-s timescale can be interpreted as the longest time it takes for dilation and stress signals to completely cross the system. At the microscopic level, this may have to do with the time it takes for liquid to migrate between the bulk and the surface. We estimate the time t it takes for flow across the diameter of the suspension a distance $2R$ as $t = 2R/U$, where the steady flow velocity U is obtained from Darcy's law as $U \approx 0.5a^2P/\eta_L R$, where is it assumed the permeability is on the order of $0.5a^2$ according to the Kozeny-Carmen equation, $\eta_L = 9 \times 10^{-4}$ Pa s is the liquid viscosity, and $a = 1.4 \times 10^{-5}$ m is the particle diameter. We estimate the driving pressure $P \approx \tau_{\max}$, as that is the expected stress at the boundary that drives rearrangement and flow in the high-stress state, and that the pressure difference acts over a distance of about the plate radius R. This yields a $t \approx 13$ s, on the same order as the observed 9-s delay time. Thus, the Darcy flow of liquid between the surface and bulk may determine the time it takes the dilation and stress signals to cross the system.

C. Reiteration of the mechanism that connects surface roughening, dilation, and stress in DST

The observation of roughening of the surface of DST suspensions when the stresses are in the high-stress range or growing indicates a coupling between stress and surface roughening and thus dilation in the shear thickening transition (Fig. 7) and high-stress state of DST (Figs. 5 and 6, Table 1). The mechanism can be explained as follows [2]. As the particle packing dilates in response to shear for $\tau > \tau_c$, it pushes against the boundaries of the suspension. Typically, the liquid-air interface is the softest boundary, which determines the macroscopic response. As dilation deforms the liquid-air interface with curvature on the order of particle size, surface tension provides a restoring force that pushes back on the particles with a maximum stress $\tau_{\max}$ that is on the order of magnitude of surface tension divided by particle size [12]. This restoring force is transmitted along an effectively frictional contact network where shear stress is proportional to normal stress, which provides the resistance to shear in the high-stress state that is observed in an apparent viscosity curve as the maximum stress $\tau_{\max}$ of the shear thickening range.

While the connection between surface roughening and the high-stress state of DST has been shown here only for cornstarch and water, similar conclusions are likely true for suspensions that exhibit similar DST, specifically those which are found to exhibit positive normal stresses, visible surface roughening (although it is not yet clear if this is visible by eye for smaller particles as they become comparable to the wavelength of light), and where the maximum stress in the shear thickening range $\tau_{\max}$ scales with surface tension divided by particle size. Notably, this scaling of $\tau_{\max}$ was confirmed for dozens of suspensions [2].

D. Consequences of boundary conditions on macroscopic behavior

The observation that high and growing stresses are coupled to surface roughening (Fig. 5, Table I) indicates that boundary conditions play a significant role in the macroscopic behavior of DST in dense suspensions. When the suspension dilates to push against the boundary, it is the softest part of the system that deforms the most and thus determines the effective stiffness of the whole and $\tau_{\max}$. Usually, the liquid-air interface is the softest boundary. On the other hand, bulk simulations usually artificially remove boundaries by using periodic boundary conditions in fixed volumes, where instead the particle stiffness provides a restoring force against dilation instead of a boundary [3,39–41]. Modified rheometer experiments with only solid boundaries have shown that $\tau_{\max}$ scales with the boundary stiffness [2]. It is likely for this reason that industrial flows of dense slurries and granular materials are often intentionally left with a free surface rather than forced through pipes with hard walls, which would produce a much larger resistance to shear.

Boundary conditions can even qualitatively affect the observed macroscopic behavior. Modified rheometer experiments have shown, for example, a flow with a constant normal stress instead of a constant rheometer gap results in an apparent shear thinning at all shear rates instead of DST for the same suspension that exhibits DST in a constant gap measurement [2,42]. This indicates that the macroscopic behavior of DST is not an inherent feature of the local constitutive relation of dense suspensions; i.e., whether or not macroscopic DST is observed in an apparent viscosity curve depends on the boundary conditions.

A common observation in DST suspensions is the spilling of the suspension, often in the form of granules that escape the surface (also known as creaming) as the liquid-air interface becomes unstable at high shear rates [34]. This happens even when shear rates are low at high packing fractions where inertia is negligible. The conditions for spillage are observed to be dependent on measurement procedure, but this tends to happen near $\tau_{\max}$, which is a major reason why reported measurements of DST curves often end near $\tau_{\max}$ and almost never go far beyond it. This can be understood if the normal stress in DST suspensions for stable flows is limited by surface tension at the liquid-air interface: A larger normal stress induced by shear resulting in dilation larger than about one particle diameter results in particles breaking through the surface, so part of the sample spills [11].

Our observation that the high-stress state of DST coincides with surface roughening at the liquid-air interface (Figs. 5 and 6, Table I) and previous observations that stresses in the high-stress state are proportional to the softest boundary stiffness for dozens of suspensions [2] and that the existence of DST in the macroscopic behavior of a particular suspension depends on boundary conditions [2,42,43] altogether indicate that the high-stress state of DST depends on boundary conditions where stresses are proportional to the softest boundary stiffness coupled to dilation. These boundary conditions in typical rheometer flows differ from the constant-volume boundary conditions typically applied to local constitutive models [4,5]. Use of unrealistic boundary conditions may lead to unrealistic results, since it has been observed that the macroscopic behavior of suspensions that exhibit DST can change radically with boundary conditions [2,42,43]. Thus, boundary conditions where stresses are proportional to the softest boundary stiffness coupled to dilation should be used in models if the intent is to describe the macroscopic behavior in the high-stress state of DST in real experimental measurements in rheometers and other flows that allow dilation [2].

E. Local constitutive relation of the high-stress state

Since we want to understand how the macroscopic behavior of the high-stress state of DST in experiments comes from the combination of boundary conditions and the local constitutive relation, we also discuss the local constitutive relation of the high-stress state of DST observed in previous work. The apparent viscosity η measured in rheometers in the high-stress state of DST (i.e., at high shear rates beyond the shear thickening range) are typically shear thinning [2,20,44,45]. This could in principle be explained either by a local constitutive relation where the main contribution to shear stress is proportional to normal stress but nearly independent of local shear rate [2,46] or by a local constitutive relation where the shear stress is proportional to local shear rate [4,5,11,46,47] in which the apparent viscosity decreases, perhaps due to an decrease in the local friction coefficient at high stress [45]. To distinguish between such proposed scalings of stress with local shear rate, measurements of shear profiles in DST suspensions with variation in shear rate either due to gravitational forces or a cylindrical Couette geometry have broken down shear stress into a component proportional to local shear rate and a component independent of local shear rate. It was found that the component dependent on local shear rate is relatively small compared to the local shear rate independent component in the shear thickening range and high-stress state [2,20,44], except in cases of high liquid viscosity where viscous forces are dominant (>700 cSt) [44]. Which scaling is dominant in average stress measurements (and what is measured as apparent viscosity in a rheometer) for a particular suspension is expected to depend on which stress scales are larger for the suspension parameters: viscous stresses (the product of shear rate, liquid viscosity, and a relative viscosity dependent on local packing fraction [4,5,11,46,47]), frictional forces independent of shear rate (the boundary stiffness per particle divided by particle size [2]), or inertial stresses (the product of density and velocity squared [2,48].

One might wonder why the viscous contribution to stresses does not blow up in the empirically observed local constitutive relation of the high-stress state if particles are being pushed into contact, when continuum hydrodynamics predicts diverging effective viscosities when particles are pushed into contact. An explanation for this observation is the breakdown of continuum hydrodynamics when there are too few liquid molecules between particles to act like a continuum fluid. This breakdown is expected to occur when the apparent viscosity becomes larger than about the ratio of particle size (or roughness scale) to liquid molecule size, corresponding to only a couple layers of liquid molecules between the large particles [1,3]. For a suspension of cornstarch in water, an upper bound on the apparent viscosity of this breakdown is 40 Pa s (the breakdown is likely at a lower apparent viscosity due to the roughness of particles) [1]. Since the high-stress state of DST occurs at higher viscosities for suspensions in cornstarch and water (2000 Pa s in Fig. 6), such a viscous hydrodynamic scaling theoretically should not apply here, as it would require the lubricating liquid to be in interparticle gaps much smaller than the size of a liquid molecule. Thus, when comparing forces to predict whether the local constitutive relation should be dominated by a viscous or frictional scaling, viscous forces are expected to be cut off at this maximum relative viscosity before the breakdown of continuum mechanics. Instead, the local shear stress in the liquid becomes dependent primarily on the normal stress like solid friction [49]. This explains the empirical observation that the shear stress is proportional to normal stress but not shear rate in the high-stress state of DST [2,20,44], where the relative viscosity tends to be high and particle size tends to be small.

If we want models to correctly describe realistic experimental DST, then the local constitutive relation for the high-stress sate should match the experimental observations that the shear stress is nearly proportional to normal stress and mostly independent of shear rate in the high-stress state [2,20,44]. In the Wyart-Cates model, constitutive relations are already separated for the high- and low-stress states, so it should be relatively easy to substitute a different constitutive relation for the high-stress state while retaining the key feature of fitting a crossover between the high- and low-stress states with an evolving fraction of frictional contacts. Some proposed local constitutive relations that would better apply to typical experiments in the high-stress state are one where shear stress is dominated by a frictional term with shear stress proportional to normal stress potentially added to weaker terms representing other significant forces [2] or the stress relation of Ref. [46] obtained from normal-stress controlled experiments, which is a boundary condition that closely approximates the observed experimental boundary condition for the high-stress state. This is not only more consistent with the measurements of the local constitutive relation of the high-stress state of DST [2,20,44] but a constitutive relation where normal stress is the main controlling factor would straightforwardly couple to dilation in the boundary conditions identified in Sec. V D.

Surface roughening is strongly correlated to shear and normal stress in DST suspensions, which fluctuate by orders of magnitude between the high- and low-stress states of DST (Fig. 5). Surface roughening is frequently found at a given observation point in the high-stress state, and two-point statistics suggest surface roughening is likely to be found at some point on the surface in high-stress state at all times. On the other hand, a complete lack of surface roughening is observed in the low-stress state when there is not rapid stress increase within the following 9 s (Table I). During the stress growth from the low-stress state to the high-stress state, surface roughening is even more likely than in the high-stress state and is observed 100% of the time following 9 s of persistent stress growth (Table I). The 9-s periods seems to correspond to the maximum time required for signals relating dilation and stress to travel across the system and may be determined by the time it takes for liquid to migrate from the surface to fill the interstices of the dilated bulk. The stress growth period can be interpreted similar to the growth portion of a material stress-strain curve where the system-spanning surface roughness is indicative of a force network that remains connected before failure, after which surface roughness is more localized in the high-stress plateau where failure occurs intermittently. While surface deformations are observed in some experiments where the high-stress state is not observed, the events are very brief and localized, so the surface roughening does not span the surface, which is required to reach the high-stress state (Table I).

We confirm that surface roughening occurs in both stress- and rate-controlled measurements in the stress range of shear thickening and the high-stress state of DST suspensions ($\tau > \tau_c$) but not in the low-stress state (Fig. 6 and 7). The numerous relationships found between surface roughening and the high-stress stress state indicate that stresses in the high-stress state of DST are coupled to surface roughening at the suspension-air interface. This coupling is explained by the argument that dilation causes particles to poke through the liquid-air interface, which responds with a restoring force from surface tension that is transmitted along a frictional particle contact network to provide the resistance to shear in the high-stress state [2]. These results confirm a need for models to include boundary conditions where normal stress comes from the stiffness of the softest boundary coupled to dilation if they are to describe the macroscopic behavior of the high-stress state of DST in real experimental measurements in rheometers and other flows that allow dilation [2].

VI. SUMMARY

Dilation can be observed on the surface of a suspension as a speckled pattern or surface roughening, as light reflects diffusively off a surface that is rough on the particle scale, which is due to dilation pushing particles through the liquid-air interface (Fig. 2, Supplemental Videos 1 and 2 [35]). Surface roughening in steady-state flows of DST suspensions is found to be intermittent and localized (Figs. 4, 8, 5), and localized regions of surface roughening can propagate along the surface of the suspension (Fig. 3, Supplemental Video 2 [35]).

ACKNOWLEDGMENTS

This work was supported by the NSF through Grant No. DMR 1410157. We thank a referee for suggesting the transition time between surface roughening and a shiny surface could be determined by the pore flow rate.

R.M. carried out initial experiments, identified the algorithm for tracking dilation, and collected data for Figs. 2–4 and 7–9. E.O. and T.P. carried out experiments with two cameras (Fig. 5 and Table I). N.K. measured viscosity curves with video (Fig. 6). R.M., E.O., T.P., and N.K. carried out the bright spot tracking and manually checked the algorithm on their respective data. E.B. conceived the project, performed statistical analyses, and wrote the paper.

APPENDIX: DETAILS OF BRIGHT PIXEL ANALYSIS

1. Obtaining the number of bright pixels *n*

We identify a quantitative measure of surface roughening from images so that we can calculate statistics and compare time series to those of stresses. Because the bright spot is a result of direct reflection off a nearly flat surface, we found that the absence of bright pixels is a good proxy for surface roughening and thus dilation. The lower panels of Fig. 2 illustrate the process of our image analysis. We first crop images as shown in Fig. 2 to remove the rheometer plates from the image while remaining large enough to contain the bright spot from the direct reflection from the light source, as well as the region it moves around in during experiments. In some experiments, where regions of surface roughening tended to be smaller than the bright spot, we cropped images down to a size smaller than the region of surface roughening so that events would consistently result in nearly zero bright pixels. We then convert the cropped grayscale images into binary black and white images. We set a brightness threshold such that pixels with greater or equal brightness values are converted to white, and pixels with lower brightness values are converted to black, as shown in the lower panels of Fig. 2, chosen to ensure that the bright reflected spot always maintains many white pixels, while regions where the surface reflection is most diffuse due to surface roughening are converted to black pixels. Once we have cropped and thresholded the image, we count the number of bright pixels n. We note that statistics of n depend on the optical and lighting setup and threshold value, so such statistics can only be meaningfully compared to other data sets with similar methods.

2. Time series of the number of bright pixels *n*

A longer time series from the same data set as Fig. 4 is shown in Fig. 8. We observe that most of the time n fluctuates in a preferred range of $\approx$200–300. The fluctuation in n is due to slight surface deformations that cause the size of the bright spot to vary. These slight fluctuations in bright spot size are visually distinct from surface roughening. Figure 8 shows five distinct surface roughening events where n drops to near zero. These surface roughening events occur intermittently, and while we sometimes observe a preferred time between events, the time series are not strictly periodic. There also appears to be a typical slope $\partial n/\partial t$ during the transitions, indicating a consistent growth rate of surface roughening regions. Each of these typical values varies with different applied stress τ or packing fraction $\phi_{\rm eff}$, although we did not systematically investigate these parameter dependences here.

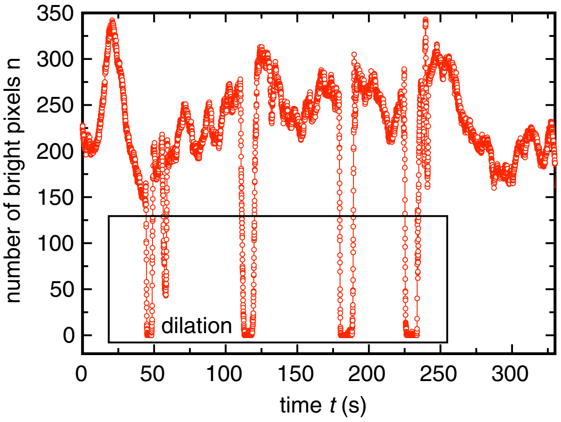

FIG. 8. Number of bright pixels n as a function of time showing several surface roughening events when n drops to near zero (indicated by the box).

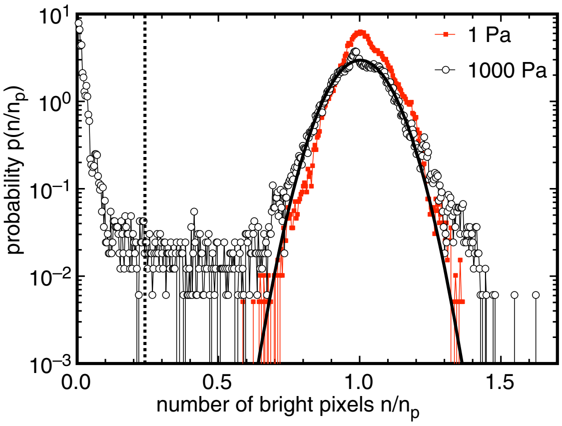

FIG. 9. Probability distribution of the number of bright pixels n. Different applied shear stresses τ are indicated in the legend. The broad peak at $n = n_p$ corresponds to a smooth suspension surface. Solid line: fit used to determine the peak location n_p. The sharp peak at $n = 0$ corresponds to a dilated state with surface roughening. Data with no visible surface roughening at $\tau = 1$ Pa do not have the peak at $n = 0$ or the low-$p(n)$ plateau. Dotted line: standard threshold value n_t/n_p below which surface roughening is counted.

3. Definition the threshold n_t for surface roughening

To obtain statistics on surface roughening, we define a threshold value of n below which surface roughening is said to occur. To identify this threshold, we use features of the probability distribution $p(n)$. A probability distribution of $p(n/n_p)$ is shown in Fig. 9 from an extended time series at $\tau = 1000$ Pa and $\phi_{\rm eff}/\phi_c = 0.905 \pm 0.008$, at the low end of the DST range. n is normalized by its value at the nonzero local maximum n_p corresponding to a smooth surface (i.e., unaffected by dilation), determined by a Gaussian fit as shown in Fig. 9. This normalization provides a scale in which experiments under different lighting conditions could potentially be compared. The peak at $n/n_p = 1$ is wide due to the fluctuations in the size of the bright spot due to slight surface deformations. The sharp peak at $n = 0$ corresponds to surface roughening (i.e., dilation) events with no bright pixels. There is a low plateau in $p(n)$ for $0.10 \lesssim n/n_p \lesssim 0.68$. This corresponds to a range that is only traversed rarely as the surface is transitioning between smooth and rough states, as seen in Figs. 4 and 8. We also confirm that data sets with no visible surface roughening have no peak in $p(n)$ at $n = 0$ or low-$p(n)$ plateau, as shown for $\tau = 1$ Pa in Fig. 9.

For the purpose of obtaining statistics on surface roughening, we define surface roughening as occurring when n is less than a threshold value $n_t = 0.24n_p$ for all data presented in this paper. This threshold value is in the low-$p(n)$ plateau for all data sets where we observe surface roughening events, even for data taken with a different camera or optical setup. While the choice of the value of n_t is somewhat arbitrary within the broad low-$p(n)$ plateau, the low probability in this plateau means that the probability of surface roughening is least sensitive to the threshold value n_t in this range. Again, because of the somewhat arbitrary nature of this threshold value, statistics can only be meaningfully compared to other data sets with the same optical and lighting setups. Distinct surface roughening events are identified as a continuous segment of the time series with $n < n_t$.

[1] E. Brown and H. M. Jaeger, Shear thickening in concentrated suspensions: Phenomenology, mechanisms, and relations to jamming, Rep. Prog. Phys. **77**, 046602 (2014).

[2] E. Brown and H. Jaeger, The role of dilation and confining stress in shear thickening of dense suspensions, J. Rheol. **56**, 875 (2012).

[3] R. Seto, R. Mari, J. F. Morris, and M. M. Denn, Discontinuous Shear Thickening of Frictional Hard-Sphere Suspensions, Phys. Rev. Lett. **111**, 218301 (2013).

[4] M. Wyart and M. E. Cates, Discontinuous Shear Thickening Without Inertia in Dense Non-Brownian Suspensions, Phys. Rev. Lett. **112**, 098302 (2014).

[5] J. F. Brady and G. Bossis, The rheology of concentrated suspensions of spheres in simple shear flow by numerical simulation, J. Fluid Mech. **155**, 105 (1985).

[6] R. L. Hoffman, Discontinuous and dilatant viscosity behavior in concentrated suspensions II. Theory and experimental tests, J. Colloid Interface Sci. **46**, 491 (1974).

[7] B. J. Maranzano and N. J. Wagner, The effects of particle size on reversible shear thickening of concentrated colloidal dispersions, J. Chem. Phys. **114**, 10514 (2001).

[8] E. Brown, N. A. Forman, C. S. Orellana, H. Zhang, B. W. Maynor, D. E. Betts, J. M. DeSimone, and H. M. Jaeger, Generality of shear thickening in suspensions, Nat. Mater. **9**, 220 (2010).

[9] A. B. Metzner and M. Whitlock, Flow behavior of concentrated (dilatant) suspensions, Trans. Soc. Rheol. **11**, 239 (1958).

[10] H. A. Barnes, Shear-thickening ("dilatancy") in suspensions of nonaggregating solid particles dispersed in Newtonian liquids, J. Rheol. **33**, 329 (1989).

[11] S. Garland, G. Gauthier, J. Martin, and J. F. Morris, Entangled granular media, J. Rheol. **57**, 71 (2013).

[12] M. E. Cates, M. D. Haw, and C. B. Holmes, Dilatancy, jamming, and the physics of granulation, J. Phys.: Condens. Matter **17**, S2517 (2005).

[13] A. Fall, F. Bertrand, G. Ovarlez, and D. Bonn, Yield Stress and Shear Banding in Granular Suspensions, Phys. Rev. Lett. **103**, 178301 (2009).

[14] A. Fall, N. Huang, F. Bertrand, G. Ovarlez, and D. Bonn, Shear Thickening of Cornstarch Suspensions as a Reentrant Jamming Transition, Phys. Rev. Lett. **100**, 018301 (2008).

[15] V. T. O'Brien and M. E. Mackay, Stress components and shear thickening of concentrated hard sphere suspensions, Langmuir **16**, 7931 (2000).

[16] M. Hermes, B. M. Guy, W. C. K. Poon, G. Poy, M. E. Cates, and M. Wyart, Unsteady flow and particle migration in dense, non-Brownian suspensions, J. Rheol. **60**, 905 (2016).

[17] Q. Xu, A. Singh, and H. M. Jaeger, Stress fluctuations and shear thickening in dense granular suspensions, J. Rheol. **64**, 321 (2020).

[18] M. I. Smith, R. Besseling, M. E. Cates, and V. Bertolla, Dilatancy in the flow and fracture of stretched colloidal suspensions, Nat. Commun. **1**, 114 (2010).

[19] M. I. Smith, Fracture of jammed colloidal suspensions, Sci. Rep. **5**, 14175 (2015).

[20] A. Fall, F. Bertrand, D. Hautemayou, C. Meziére, P. Moucheront, A. Lemaître, and G. Ovarlez, Macroscopic Discontinuous Shear Thickening Versus Local Shear Jamming in Cornstarch, Phys. Rev. Lett. **114**, 098301 (2015).

[21] N. M. James, E. Han, R. A. Lopez de la Cruz, J. Jureller, and H. M. Jaeger, Interparticle hydrogen bonding can elicit shear jamming in dense suspensions, Nat. Mater. **17**, 965 (2018).

[22] M. Roché, E. Myftiu, M. C. Johnston, P. Kim, and H. A. Stone, Dynamic Fracture of Nonglassy Suspensions, Phys. Rev. Lett. **110**, 148304 (2013).

[23] B. Allen, B. Sokol, S. Mukhopadhyay, R. Maharjan, and E. Brown, Structure of the system-spanning dynamically jammed region in response to impact of cornstarch and water suspensions, Phys. Rev. E **97**, 052603(2018).

[24] R. Maharjan, S. Mukhopadhyay, B. Allen, T. Storz, and E. Brown, Constitutive relation of the system-spanning dynamically jammed region in response to impact of cornstarch and water suspensions, Phys. Rev. E **97**, 052602(2018).

[25] S. Mukhopadhyay, B. Allen, and E. Brown, Testing constitutive relations by running and walking on cornstarch and water suspensions, Phys. Rev. E **97**, 052604 (2018).

[26] D. Lootens, H. Van Damme, and P. Hébraud, Giant Stress Fluctuations at the Jamming Transition, Phys. Rev. Lett. **90**, 178301 (2003).

[27] D. Lootens, H. van Damme, Y. Hémar, and P. Hébraud, Dilatant Flow of Concentrated Suspensions of Rough Particles, Phys. Rev. Lett. **95**, 268302 (2005).

[28] V. Rathee, D. L. Blair, and J. S. Urbach, Localized stress fluctuations drive shear thickening in dense suspensions, Proc. Nat. Acad. Sci. USA **114**, 8740 (2017).

[29] V. Rathee, D. L. Blair, and J. S. Urbach, Localized transient jamming in discontinuous shear thickening, J. Rheol. **64**, 299 (2020).

[30] B. Saint-Michel, T. Gibaud, and S. Manneville, Uncovering Instabilities in the Spatiotemporal Dynamics of a Shear-Thickening Cornstarch Suspensionn, Phys. Rev. X **8**, 031006 (2018).

[31] R. N. Chacko, R. Mari, M. E. Cates, and S. M. Fielding, Dynamic Vorticity Banding in Discontinuously Shear Thickening Suspensions, Phys. Rev. Lett. **121**, 108003 (2018).

[32] G. Ovarlez, A. V. Nguyen Le, W. J. Smit, A. Fall, R. Mari, G. Chatt'e, and A. Colin, Density waves in shear-thickening suspensions, Sci. Adv. **6**, 5589 (2020).

[33] R. Maharjan and E. Brown, Effective packing fraction for better resolution near the critical point of shear thickening suspensions, Phys. Rev. E **99**, 042604 (2019).

[34] D. J. M. Hodgson, M. Hermes, E. Blanco, and W. C. K. Poon, Granulation and suspension rheology: A unified treatment, arXiv:1907.10980.

[35] See Supplemental Material at http://link.aps.org/supplemental/10.1103/PhysRevE.103.012603 for videos and other details.

[36] We use the raw measurement ϕ_{wt} instead of ϕ_{eff} here because the fit to define ϕ_{eff} was not done for such a small gap [33].

[37] E. Brown and H. M. Jaeger, Dynamic Jamming Point for Shear Thickening Suspensions, Phys. Rev. Lett. **103**, 086001 (2009).

[38] E. Brown, H. Zhang, N. A. Forman, B. W. Maynor, D. E. Betts, J. M. DeSimone, and H. M. Jaeger, Shear thickening and jamming in densely packed suspensions of different particle shapes, Phys. Rev. E **84**, 031408 (2011).

[39] R. Mari, R. Seto, J. F. Morris, and M. M. Denn, Shear thickening, frictionless, and frictional rheologies in non-Brownian suspensions, J. Rheol. **58**, 1693 (2014).

[40] C. Heussinger, Shear thickening in granular suspensions: Interparticle friction and dynamically correlated clusters, Phys. Rev. E **88**, 050201(R) (2013).

[41] R. Seto, G. Giusteri, and A. Mariniello, Microstructure and thickening of dense suspensions under extensional and shear flows, J. Fluid Mech. **825**, R3 (2017).

[42] A. Fall, F. Bertrand, G. Ovarlez, and D. Bonn, Shear thickening of cornstarch suspensions, J. Rheol. **56**, 575 (2012).

[43] J. Dong and M. Trulsson, Analog of discontinuous shear thickening flows under confining pressure, Phys. Rev. Fluids **2**, 081301(R) (2017).

[44] Q. Xu, E. Brown, and H. M. Jaeger, Shear thickening in highly viscous granular suspensions, EPL **107**, 68004 (2014).

[45] G. Chatté, J. Comtet, A. Niguès, L. Bocquet, A. Siria, G. Ducouret, F. Lequeux, N. Lenoir, G. Ovarlez, and A. Colin, Shear thinning in non-Brownian suspensions, Soft Matter **14**, 879 (2018).

[46] F. Boyer, E. Guazzelli, and O. Pouliquen, A Constitutive Law for Dense Granular Flows, Phys. Rev. Lett. **107**, 188301 (2011).

[47] H. Nakanishi and N. Mitarai, Shear thickening oscillation in a dilatant fluid, J. Phys. Soc. Japan **80**, 033801 (2011).

[48] J. Dong and M. Trulsson, Unifying viscous and inertial regimes of discontinuous shear thickening suspensions, J. Rheol. **64**, 255 (2020).

[49] J. Van Alsten and S. Granick, Molecular Tribometry of Ultrathin Liquid Films, Phys. Rev. Lett. **61**, 2570 (1988).